An upper bound for extreme temperatures over midlatitude land

Yi Zhang*[1,2], William R. Boos [1,3]

[1] Department of Earth and Planetary Science, University of California, Berkeley

[2] Miller Institute for Basic Research in Science, University of California, Berkeley

[3] Climate and Ecosystem Sciences Division, Lawrence Berkeley National Laboratory

*Correspondence to: y-zhang@berkeley.edu

Abstract

Heatwaves damage societies globally and are intensifying with global warming. Several mechanistic drivers of heatwaves, such as atmospheric blocking and soil moisture-atmosphere feedback, are well-known for their ability to raise surface air temperature. However, what limits the maximum surface air temperature in heatwaves remains unknown; this became evident during recent Northern Hemisphere heatwaves which achieved temperatures far beyond the upper tail of the observed statistical distribution. Here, we present the hypothesis, with corroborating evidence, that convective instability limits annual maximum surface air temperatures (TXx) over midlatitude land. We provide a theory for the upper bound of midlatitude temperatures, which accurately describes the observed relationship between temperatures at the surface and in the mid-troposphere. Known heatwave drivers shift the position of the atmospheric state in the phase space described by the theory, changing its proximity to the upper bound. Our theory suggests that the upper bound for midlatitude TXx should increase 1.9 times as fast as 500-hPa temperatures. Using empirical 500-hPa warming, we project that the upper bound of TXx over Northern Hemisphere midlatitude land (40°N-65°N) will increase about twice as fast as global mean surface air temperature, and TXx will increase faster than this bound over regions that dry on the hottest days.

1 Introduction

Recent mega-heatwaves—the 2010 Russian heatwave,[7] the 2019 European heatwave,[8] and the 2021 Western North America heatwave[9]—set temperature records more than three standard deviations beyond the local long-term mean of annually hottest daily maximum temperatures

(TXx; Fig. 1a). The 2010 Russian heatwave (Fig. 1d), accompanied by severe drought and wildfires, caused thousands of deaths, while the 2019 European heatwave (Fig. 1c) exceeded the memorable 2003 heatwave, setting records in Western Europe. The 2021 Western North America heatwave (Fig. 1b), arguably the most anomalous heatwave recorded, exceeded the previous record by 5°C. Moreover, temperatures in this event broke from the upper tail of the distribution of recorded extreme temperatures, preventing a reliable statistical assessment of its likelihood[9] and calling for a revised physical understanding of heatwaves.

Previous studies identified multiple physical processes involved in midlatitude heatwaves. A prerequisite is an atmospheric anticyclone,[2] with clockwise flow (in the Northern Hemisphere) around a high-pressure center. Subsiding air within anticyclones warms through compression, prohibiting clouds and allowing sunlight to heat the surface;[3] poleward flow in the anticyclone can also transport hotter air into the heatwave.[10] Anticyclones usually drift eastward following midlatitude westerly winds, but can stall over a region in a phenomenon known as blocking, which is especially favorable to heatwaves.[2] Natural modes of variability that modulate the occurrence and movement of anticyclones thus affect heatwaves.[11–15] Beneath anticyclones, land-atmosphere feedbacks can enhance heatwaves,[4,16,17] with warmer air drying soils, which in turn limit surface evaporative cooling and warm surface air more.[5,6,18] Processes that affect soil moisture, such as antecedent precipitation and evapotranspiration,[19,20] therefore affect heatwave severity.

Different heatwaves have been attributed to different processes,[21–24] and we lack a general theory for midlatitude heatwave intensity. This lack of general understanding is exemplified by the inability to explain the extreme nature of the 2021 Western North America heatwave in terms of the aforementioned processes.[9] Furthermore, we do not know whether different

processes can interact nonlinearly to amplify heatwaves. All of these facts impede accurate future projections.[25]

2 Physical mechanism and theory

We first present a hypothesis, and associated evidence, for the mechanism that limits surface air temperatures over midlatitude land. Specifically, we hypothesize that convective instability halts heatwave development. Surface air temperature cannot increase indefinitely during heatwaves, but can only rise till the atmospheric temperature profile becomes unstable to convection, which with any associated precipitation would cool the land surface. This hypothesis requires the free-tropospheric temperature profile to be at least episodically near neutral to moist convection, which is an accurate assumption for the tropical atmosphere in general[26,27] and tropical heat extremes in particular.[28,29] Moist convective neutrality also holds for midlatitude land in summer,[30,31] however the implications of this neutrality for heatwaves has not been studied.

We examine this hypothesis using a composite analysis of all annual hottest daily maximum temperatures (TXx) over land between 40°N and 65°N in 2010 (choosing other years does not affect results). We take the time series of a climate variable over a 21-day window centered on the day of TXx for each location, then average the time series of all locations. The resulting composites (Fig. 2) thus show the structural characteristics of many heat events. Supporting the convective instability hypothesis, convective available potential energy (CAPE), which is a measure of convective instability, peaks on the annual hottest day (day 0). Consequently, precipitation increases on day 0, then surface air temperature drops

as precipitation peaks on day 1. The drop of surface air temperature occurs faster than its build-up, consistent with the hypothesis that the fast processes of convection and precipitation rapidly cool the land surface. These composites identify precipitating convection as a common conclusion of heat events over midlatitude land, motivating application of theories for moist convective stability.

Convective instability can be estimated by comparing surface air moist static energy (MSE) to the free-tropospheric saturation MSE, with the difference between these quantities near zero in the event of convection. MSE depends on temperature (T), specific humidity (q), and geopotential height (z):

$$\mathrm{MSE} = c_p T + L_v q + g z \tag{1}$$

where c_p is the specific heat of air at constant pressure, L_v is the latent heat of vaporization, and g is the gravitational acceleration. Surface air temperature can build in a stable column where surface air MSE (MSE_s) does not exceed free-tropospheric saturation MSE (MSE_a^*):

$$\mathrm{MSE_s} \leq \mathrm{MSE_a^*}. \tag{2}$$

Using the 500-hPa level to represent the free troposphere (Methods), we find that midlatitude TXx events satisfy equation (2), with MSE_s only high enough to reach MSE_{500}^* on the hottest day (Fig. 2). Combining equations (1) and (2), and thermodynamic relations, we obtain an upper bound of surface air temperature (T_s; see Methods for derivation):

$$T_s \leq T_{500} + \frac{L_v}{c_p} q_{\mathrm{sat}}(T_{500}) + \frac{g\overline{z_{500}}}{c_p \overline{T_{500}}} T_{500} - \frac{g}{c_p} z_s, \tag{3}$$

where T_{500} is 500-hPa temperature, $q_{\mathrm{sat}}(T_{500})$ is 500-hPa saturation specific humidity, $\overline{T_{500}}$ and $\overline{z_{500}}$ are 500-hPa constant climatological values (see Methods), and z_s is surface elevation.

Equation (3) states that the highest possible T_s is determined by T_{500}, offset by z_s. The T_s upper bound is achieved when the energy in MSE_s is entirely allocated to temperature and surface air specific humidity is zero.

3 Observational evidence

We now assess the consistency of observations with the upper bound expressed by equation (3), examining $T_s + \frac{g}{c_p} z_s$ instead of T_s so that locations with different surface elevations can be readily compared. We show the joint distribution of $T_s + \frac{g}{c_p} z_s$ and T_{500} over land between 40°N and 65°N (Fig. 3a; Methods). The theory accurately delineates the highest observed $T_s + \frac{g}{c_p} z_s$ for each T_{500} (Fig. 3a). Few data points fall above the T_s upper bound, where (T_s, T_{500}) pairs would produce convective instability. This analysis only includes the Northern Hemisphere because the same latitudes in the Southern Hemisphere are mostly covered by ocean.The agreement between theory and observations (Fig. 3a) suggests T_{500} as the limiting factor of T_s, providing new insight on midlatitude heatwaves.

We argued for a top-down control on T_s by T_{500}, but causation is not apparent from Fig. 3a. To rule out the alternative possibility that T_s controls T_{500} through convective heating, we examine the time series of heat events. The 500-hPa saturation MSE (MSE^*_{500}), which strongly depends on T_{500}, peaks the day before TXx and remains at a similar level on the day of TXx (Fig. 2). If T_s controlled T_{500} through convective heating, MSE^*_{500} would peak after T_s and the onset of precipitation. Furthermore, individual heatwaves highlighted in Fig. 1b-d were preceded by warm anomalies confined to the atmospheric layer between 300 hPa - 700 hPa, and are succeeded by precipitation (Extended Data Fig. 1). These time

series support the hypothesis that T_{500} controls T_s in midlatitude heat extremes, not the other way around.

4 Connection to well-known heatwave drivers

We demonstrate how the convective-instability mechanism can be used to understand the influence of anticyclones and soil moisture on heatwaves. We use 500-hPa relative vorticity from reanalysis as a proxy for anticyclone strength, with negative values being anticyclonic in the Northern Hemisphere. As expected, 500-hPa relative vorticity is anti-correlated with T_{500} (Fig. 3b), because when warmer air moves poleward conserving potential vorticity, its relative vorticity becomes more negative as planetary vorticity increases. In the T_s-T_{500} phase space, anticyclones make warmer T_s possible by moving the atmospheric state to larger T_{500}. However, the actual T_s achieved in an anticyclone ranges from the upper bound to tens of degrees Celsius below that bound, indicating that strong anticyclones are necessary but insufficient for high T_s.

To investigate the role of soil moisture, we examine daily mean volumetric surface (0-7 cm) soil water content from reanalysis averaged over the antecedent 30 days (the reanalysis used here,,[?] assimilates soil moisture observations and represents soil moisture better than previous reanalyses; for shallow soil moisture it has comparable skill to the dynamically downscaled land product ERA5-Land[33,34]). Antecedent surface soil water content at a given T_{500} is anti-correlated with T_s, with a gradient in T_s-T_{500} space that is nearly orthogonal to that of relative vorticity (Fig. 3c). In our convective-instability framework, the role of soil moisture is that dryer soil leads to lower surface air specific humidity (q_s) and a

partitioning of MSE_s towards temperature, consistent with the soil moisture-atmosphere feedback;[4–6,16–18] since the T_s upper bound is only met at zero q_s (Methods), lowering q_s moves the actual T_s toward the upper bound.

To summarize, free-tropospheric anticyclones allow access to larger values of T_s by increasing T_{500} (rightward movement in the T_s-T_{500} phase space), while low antecedent soil moisture allows the actual T_s to approach the upper bound by lowering q_s (upward movement in the phase space). Variations in anticyclone strength and soil moisture align with nearly orthogonal dimensions in the T_s-T_{500} phase space; neither factor alone ensures a heatwave, while neither factor has to be extreme to result in an extreme heatwave.

5 Insight into recent heatwaves

The theory can be applied to the three recent mega-heatwaves in Western North America, Western Europe, and Western Russia (Fig. 3d-f). These regions have moderately humid summers, therefore the joint T_s-T_{500} distributions are offset below the upper bound (which assumes zero q_s). If we lower the upper bound by the lowest q_s achieved over 1979-2021 for each region, the maximum T_s then better tracks the adjusted upper bound (Extended Data Fig. 2).

Our theory explains the extreme nature of the 2021 Pacific Northwest heatwave, where the highest T_s (29 June 2021) broke the previous record (22 July 2006) by 5 K even though anomalies of commonly analyzed quantities (500-hPa geopotential height, antecedent precipitation) were mild.[9] For this event, T_{500} on 29 June 2021 reached 268.2 K, exceeding the 22 July 2006 value by 2.2 K (Fig. 3d), which amounts to a 4.5-K increase in the T_s upper bound

by equation (3). Therefore, the T_{500} anomaly alone explains most of the 5-K T_s anomaly, and antecedent soil moisture plays a minor role (Extended Data Fig. 2a).

For the 2019 Western Europe heatwave (Fig. 3e), T_{500} was 1.3 K higher than the hottest day during the 2003 European heatwave, translating to a 2.5 K increase in the T_s upper bound. The actual T_s only broke the 2003 record by 1.5 K, consistent with the fact that q_s was higher in the 2019 heatwave. Neither T_{500} nor soil moisture (Extended Data Fig. 2b) broke previous records; T_{500} for this event ranked at the top 1.5% and soil water content ranked at the bottom 2% for this region in summer months. This heatwave thus exemplifies the aforementioned near-orthogonal interaction between anticyclone strength and soil moisture in the T_s-T_{500} phase space.

The 2010 Russian heatwave (Fig. 3f) was driven by desiccated soil (Extended Data Fig. 2c) after prolonged blocking. Antecedent soil water content for the hottest days of this heatwave was 36% less than the summer average and 26% less than the summer minimum of other years for the same region, while T_{500} only ranked at the 93rd percentile of summer daily T_{500} for the region. Compared to the hottest summer day in 2021, the excess T_{500} in 2010 only translates to 2.5 K of increase in the T_s upper bound, but the actual T_s was higher in 2010 by 3.9 K due to desiccated soil; movement in the T_s-T_{500} phase space was mainly upward relative to the historical distribution.

6 Trends of annual hottest daily maximum temperatures

We now examine the consistency of historical temperature trends with our theory. The increase of the T_s upper bound ($T_{s,\max}$) per unit warming of T_{500} can be obtained by differentiating equation (3):

$$\frac{\mathrm{d}T_{s,\max}}{\mathrm{d}T_{500}} = 1 + \frac{L_v}{c_p}\frac{\mathrm{d}q_{\mathrm{sat}}(T_{500})}{\mathrm{d}T_{500}} + \frac{g\overline{z_{500}}}{c_p\overline{T_{500}}}. \tag{4}$$

$$(\text{Magnitude}: 1 \qquad 0.39 \sim 1.11 \qquad 0.21)$$

Equation (4) is nonlinear in T_{500} due to the near-exponential dependence of q_{sat} on temperature, so the sensitivity of $T_{s,\max}$ to T_{500} is larger at warmer temperatures (Fig. 3). The increase in $T_{s,\max}$ induced by T_{500} warming is always larger than the T_{500} warming itself, due to contributions from Clausius-Clapeyron (second term on the right hand side of equation (4)) and the geopotential (third term). The Clausius-Clapeyron term ranges from 0.39 to 1.11 in the present climate. The 500-hPa geopotential anomaly, though frequently analyzed for heatwaves, plays a minor role, contributing about one-fifth that of temperature (first term) and about one-fifth to half that of the Clausius-Clapeyron term. Taking T_{500} as 262 K, which is the most common T_{500} value on the annual hottest days over midlatitude land in the present climate, we find the increase in the T_s upper bound per unit T_{500} warming ($\frac{\mathrm{d}T_{s,\max}}{\mathrm{d}T_{500}}$) to be 1.86.

We compare this theoretical ratio with observations and reanalysis. From 1979 to 2021, the warming of TXx averaged over land between 40°N and 65°N is 1.9 times that of T_{500}

on such days, from ERA5 reanalysis, with T_{500} increasing at 0.19±0.06 K/decade and TXx 0.36±0.06 K/decade (Fig. 4a, b). TXx from HadEX3[42] gridded station observations increased by 0.32±0.06 K/decade from 1979 to 2018, and T_{500} from ERA5 for the same period increased 0.18±0.06 K/decade, with the ratio of the two being 1.8. These similar ratios show that Northern Hemisphere midlatitude TXx increased over recent decades at a rate that agrees strongly with equation (4).

In addition, the spatial pattern of TXx trends resembles that of the T_s upper bound calculated by multiplying the local trend of T_{500} on annual hottest days with the local value of $\frac{\mathrm{d}T_{s,\max}}{\mathrm{d}T_{500}}$ from equation (4). The negative trends of TXx over the Eastern United States and Central Asia correspond to the cooling of T_{500} on the hottest days over those regions (Fig. 4c, d).

The similar warming trends of TXx and the upper bound of T_s suggest that changes in surface air specific humidity (q_s) on the annual hottest days played a minor role in the trend of TXx. Drying or moistening of the hottest days should deviate increases in TXx from the prediction by equation (4). Consistently, the hottest days over most Northern Hemispheric midlatitude land have not seen significant moistening or drying over recent decades (Extended Data Fig. 4a, c), despite the robust increase in annual mean q_s (Extended Data Fig. 4b, d). Though there is uncertainty in q_s data, this result is in line with recent work finding that q_s on the hottest days has a muted increase[35] and has even decreased over certain regions.[36]

7 Discussion and Implication

We presented evidence from multiple observational sources supporting the hypothesis that convective instability limits peak surface air temperatures over midlatitude land, and we developed a theory that explains the observed relationship between the peak surface air temperature (T_s) and 500-hPa temperature (T_{500}). This mechanism, focusing on the termination of heatwaves, complements previous descriptions of processes active in the developing phase of heatwaves, providing an upper-bound for heatwaves that is a curve in T_s-T_{500} space. The direction of causality between T_s and T_{500} is important; T_{500} warms while convection is suppressed before T_s peaks, then precipitation begins when surface air MSE becomes large enough to satisfy a simple criterion for convective instability ($\mathrm{MSE}_s \geq \mathrm{MSE}_a^*$).

Several caveats exist. First, our theory assumes convective plumes have no exchange with the environment, but entrainment of environmental air could affect convective onset.[37,38] This may not change the first-order picture for all midlatitude land (Fig. 3a), but could alter behavior for certain regions. Second, though most locations receive considerable rainfall following heat events, precipitation following heatwaves is much less over dry regions, such as in Central Asia and the Midwestern United States. The absence of notable precipitation, which could be due to evaporation of falling condensate, does not necessarily contradict the convective-instability mechanism, but further investigation is merited in arid regions. Third, our mechanism does not address the frequency of extreme temperatures; extensions of our theory may provide new insight on heatwave frequency.

A natural next step is to estimate how the upper bound of T_s will increase with future global warming. On the annual hottest days in recent decades, T_{500} (from ERA5) has

warmed at a similar rate as both annual mean T_{500} over Northern Hemispheric midlatitude land and global mean surface air temperature (the latter values were drawn from multiple observational datasets;[39,40,43] Extended Data Table 1 and Fig. 4b). Given this, the T_s upper bound over midlatitude land should on average increase around twice as fast as global mean surface air temperature. Regional increases of the T_s upper bound depend on the base-state values and warming patterns of T_{500}. Regions of warmer T_{500} in the base climate should expect more increase in the T_s upper bound given the same T_{500} warming (Fig. 3), due to the Clausius-Clapeyron nonlinearity in equation (4).

A related question is how TXx will change relative to the upper bound of T_s, and the answer depends on q_s. Regions that dry on the hottest days should expect a faster increase in TXx than the upper bound. Our results therefore identify two factors that must be constrained for accurate projection of midlatitude extreme temperatures: i) the amount of midlatitude free-tropospheric warming, and ii) surface air specific humidity changes on the hottest days. Understanding the physical processes controlling these factors should be priority in future research on midlatitude extreme temperatures.

Methods

Derivation of the upper bound of surface air temperature. Combining equation (2) and equation (1), we have

$$c_p T_s + L_v q_s + g z_s \leq c_p T_{500} + L_v q_{\text{sat}}(T_{500}) + g z_{500}, \tag{5}$$

where T_s, q_s, and z_s are temperature, specific humidity, and elevation at the surface, T_{500}, $q_{\text{sat}}(T_{500})$, and z_{500} are temperature, saturation specific humidity, and height at the 500-hPa pressure surface, c_p of 1004.7090 J/kg/K is the specific heat capacity of air at constant pressure, L_v of 2.5008×10^6 J/kg is the latent heat of vaporization, and g is gravity which equals 9.81 m/s^2.

We then write $q_{\text{sat}}(T_{500})$ and z_{500} as functions of T_{500}, namely

$$q_{\text{sat}}(T_{500}) \simeq \frac{\epsilon e_{\text{sat}}(T_{500})}{500 \text{ hPa}}, \tag{6}$$

where ϵ is the molar ratio between water vapor and dry air, e_{sat} is the saturation vapor pressure given by the Clausius-Clapeyron equation, and

$$z_{500} = \frac{\overline{z_{500}}}{\overline{T_{500}}} T_{500}, \tag{7}$$

where $\overline{z_{500}}$ and $\overline{T_{500}}$ are climatological geopotential height and temperature at 500 hPa, taking the values of 5.682 km and 258.8 K, respectively.

While equation (6) is apparent, equation (7) requires some elaboration. Combining hydrostatic balance $\mathrm{d}p/\mathrm{d}z = -\rho g$ and the ideal gas law $p = \rho R T$, we have

$$\mathrm{d} \ln p = -\frac{g}{RT} \mathrm{d}z, \tag{8}$$

where p is pressure, R is the ideal gas constant of dry air, with a value of 287.058 J/kg/K. We integrate equation (8) from the surface (using a nominal value of 1000 hPa) to 500 hPa, yielding

$$\ln \frac{1000 \text{ hPa}}{500 \text{ hPa}} = \ln 2 = \frac{g}{R} \int_0^{z_{500}} \frac{\mathrm{d}z}{T}. \tag{9}$$

We approximate the atmospheric temperature structure as having a constant lapse rate Γ, i.e.,

$$T = -\Gamma(z - z_{500}) + T_{500}, \tag{10}$$

and thus we can integrate equation (8) to get

$$\ln 2 = \frac{g}{R\Gamma} \ln \frac{T_{500}}{\Gamma z_{500} + T_{500}}. \tag{11}$$

The climatological values $\overline{T_{500}}$ and $\overline{z_{500}}$ should also satisfy equation (9):

$$\ln 2 = \frac{g}{R\Gamma} \ln \frac{\overline{T_{500}}}{\Gamma \overline{z_{500}} + \overline{T_{500}}}. \tag{12}$$

Equation (11) and (12) together give equation (7).

Substituting equation (7) into equation (5), we have

$$c_p T_s + g z_s \le c_p T_{500} + L_v q_{\text{sat}}(T_{500}) + \frac{g\overline{z_{500}}}{\overline{T_{500}}} T_{500} - L_v q_s. \tag{13}$$

We take the maximum of the right hand side of equation (13) by setting q_s to zero and thus obtain the upper bound of T_s:

$$T_s + \frac{g}{c_p} z_s \le T_{500} + \frac{L_v}{c_p} q_{\text{sat}}(T_{500}) + \frac{g\overline{z_{500}}}{c_p \overline{T_{500}}} T_{500}. \tag{14}$$

Choice of the 500-hPa pressure level. The pressure level we choose to represent the free troposphere in the theory should be between the planetary boundary layer (PBL) top

and the level of neutral buoyancy (LNB). This level should be far enough from the PBL to not be affected by the surface air temperature, otherwise our theory assuming free-tropospheric control on surface air temperature would not stand; this level should also be frequently coupled to the surface through convection and should be reached by most convective events in summer. The daily-maximum PBL height between 40°N and 65°N on the annual hottest days is around 2 km and could be 5 km over dry areas (based on ERA5), which translates to a PBL top between 550 hPa and 800 hPa. The LNB (calculated from ERA5 hourly data) for summer months between 40°N and 65°N mostly ranges from 250 hPa to 500 hPa. Figures in ref.[30] also show that convective neutrality extends to the midtroposphere for a substantial fraction of time over Northern Hemispheric land in summer. Therefore, we choose the 500-hPa pressure level to represent the free troposphere in Eq. (1), as it satisfies the two aforementioned requirements.

Ground observations. The HadGHCND dataset provides the anomalies of daily maximum temperatures (TX) on a $2.5° \times 3.75°$ spatial grid relative to the 1961-1990 climatology. We create a daily TX climatology using ERA5 data interpolated to the coarser grid of HadGHCND.

Data Availability

The ERA5 hourly data on pressure levels and single levels from 1979 to present were downloaded from the Copernicus Climate Change Service Climate Data Store (`https://cds.climate.copernicus.eu`). GPM data were downloaded from the NASA Goddard Earth Sciences Data and Information Services Center (`https://disc.gsfc.nasa.gov/datasets/`

GPM_3IMERGDF_06/summary). HadCRUT5 data were provided by Met Office Hadley Centre and downloaded from https://www.metoffice.gov.uk/hadobs/hadcrut5/data/current/download.html. HadEX3 data were provided by Met Office Hadley Centre and downloaded from https://www.metoffice.gov.uk/hadobs/hadex3/. HadGHCND gridded daily temperatures were provided by Met Office Hadley Centre and downloaded from https://www.metoffice.gov.uk/hadobs/hadghcnd/. IUKv2 radiosonde data were provided by Steven Sherwood. MSU/AMSU data produced by Remote Sensing Systems were downloaded from https://www.remss.com/measurements/upper-air-temperature/.

Code Availability

The computer code used in this paper is available from the corresponding author.

References

[1] Sonia, I. Seneviratne *et al.* in *Climate Change 2021: The Physical Science Basis. Contribution of Working Group I to the Sixth Assessment Report of the Intergovernmental Panel on Climate Change* (eds Masson-Delmotte, V. et al.) Ch. 11 (IPCC, 2021)

[2] Pfahl, S., & Wernli, H. Quantifying the relevance of atmospheric blocking for co-located temperature extremes in the Northern Hemisphere on (sub-) daily time scales. *Geophys. Res. Lett.* **39**, L12807(2012).

[3] Bieli, M., Pfahl, S., & Wernli, H. A Lagrangian investigation of hot and cold temperature extremes in Europe. *Q. J. R. Meterorol. Soc.* **141**, 98-108(2015).

[4] Huang, J., van den Dool, H.M., & Georgarakos, K.P. Analysis of model-calculated soil moisture over the United States (1931–1993) and applications to long-range temperature forecasts. *J. Climate* **9**, 1350-1362(1996).

[5] Fischer, E.M. *et al.* Contribution of land-atmosphere coupling to recent European summer heat waves. *Geophys. Res. Lett.* **34**, L06707(2007).

[6] Seneviratne, S.I. *et al.* Investigating soil moisture–climate interactions in a changing climate: A review. *Earth Sci. Rev.* **99**, 125-161(2010).

[7] Grumm, Richard H. The central European and Russian heat event of July–August 2010. *Bull. Am. Meteorol. Soc.* **92**, 1285-1296(2011).

[8] Mitchell, Dann *et al.* The day the 2003 European heatwave record was broken. *Lancet Planet. Health.* **3** e290-e292(2019).

[9] Philp, S.Y. *et al.* Rapid attribution analysis of the extraordinary heatwave on the Pacific Coast of the US and Canada June 2021. *Earth Syst. Dyn. Discuss.* [preprint], `https://doi.org/10.5194/esd-2021-90,inreview,2021.`.

[10] Schumacher, D.L., Keune, J., van Heerwaarden, C.C. et al. Amplification of mega-heatwaves through heat torrents fuelled by upwind drought. *Nat. Geosci.* **12**, 712–717 (2019).

[11] Kenyon, J., & Hegerl, G.C. Influence of modes of climate variability on global temperature extremes. *J. Climate* **21**, 3872-3889(2008).

[12] Arblaster, J.M., & Alexander, L.V. The impact of the El Niño-Southern Oscillation on maximum temperature extremes. *Geophys. Res. Lett.*, **39**, L20702(2012).

[13] Horton, D., *et al.* Contribution of changes in atmospheric circulation patterns to extreme temperature trends. *Nature* **522**, 465–469 (2015)

[14] Grotjahn, R. *et al.* North American extreme temperature events and related large scale meteorological patterns: a review of statistical methods, dynamics, modeling, and trends. *Clim. Dyn.* **46**, 1151–1184 (2016).

[15] Li, M. *et al.* Collaborative impact of the NAO and atmospheric blocking on European heatwaves, with a focus on the hot summer of 2018. *Environ. Res. Lett.* **15**, 114003(2020).

[16] Durre, I., Wallace, J.M., & Lettenmaier D.P. Dependence of Extreme Daily Maximum Temperatures on Antecedent Soil Moisture in the Contiguous United States during Summer. *J. Climate* **13**, 2641–2651(2000).

[17] Brabson, S.Y. *et al.* Soil moisture and predicted spells of extreme temperatures in Britain. *J. Geophys. Res. Atmos.* **110**, D05104(2005).

[18] Seneviratne, S.I. *et al.* Land–atmosphere coupling and climate change in Europe *Nature* **443**, 205-209(2006).

[19] Eltahir, E.A. A soil moisture–rainfall feedback mechanism: 1. Theory and observations. *Water Resour. Res.* **34**, 765-776(1998).

[20] Betts, A.K. Understanding hydrometeorology using global models. *Bull. Amer. Meteorol. Soc.* **85**, 1673-1688(2004).

[21] Black, E. *et al.* Factors contributing to the summer 2003 European heatwave. *Weather* **59**, 217-223(2004).

[22] Miralles, D.G. *et al.*. Mega-heatwave temperatures due to combined soil desiccation and atmospheric heat accumulation. *Nat. Geosci.* **7** 345-349(2014).

[23] Wehrli, K. *et al.* Identifying key driving processes of major recent heat waves. *J. Geophys. Res. Atmos.* **124**, 11746-11765(2019).

[24] Xu, P. *et al.* Disentangling dynamical and thermodynamical contributions to the record-breaking heatwave over Central Europe in June 2019. *Atmos. Res.* **252**, 105446(2021).

[25] Horton, R.M. *et al.* A Review of Recent Advances in Research on Extreme Heat Events. *Curr. Clim. Change Rep.* **2**, 242–259 (2016).

[26] Xu, K.M., & Emanuel, K.A. (1989). Is the tropical atmosphere conditionally unstable?. *Mon. Weather Rev.* **117**, 1471-1479(1989).

[27] Emanuel, K.A., Neelin, D.J., & Bretherton, C.S. On large-scale circulations in convecting atmospheres. *Q. J. R. Meteorol. Soc.* **120** 1111-1143(1994).

[28] Zhang, Y., Held, I., & Fueglistaler, S. Projections of tropical heat stress constrained by atmospheric dynamics. *Nat. Geosci.* **14**, 133-137(2021).

[29] Byrne, M.P. Amplified warming of extreme temperatures over tropical land. *Nat. Geosci.* **14**, 837–841 (2021)

[30] Korty, R. L., & Schneider, T. A climatology of the tropospheric thermal stratification using saturation potential vorticity. *J. Clim.* **20**, 5977-5991(2007).

[31] Miyawaki, O., Shaw, T., & Jansen, M. Quantifying energy balance regimes in the modern climate, their link to lapse rate regimes, and their response to warming. *J. Clim.* **35**, 1045–1061(2022).

[32] Hersbach, H. *et al.* The ERA5 global reanalysis. *Q. J. R. Meteorol. Soc.* **146**, 1999-2049(2020).

[33] Li, M., Wu, P., & Ma, Z. A comprehensive evaluation of soil moisture and soil temperature from third-generation atmospheric and land reanalysis data sets. *Int. J. Climatol* **40** 5744-5766(2020).

[34] Muñoz-Sabater, J. *et al.* ERA5-Land: A state-of-the-art global reanalysis dataset for land applications. *Earth Syst. Sci. Data* **13** 4349-4383(2021).

[35] Coffel, E.D. *et al.* Nonlinear increases in extreme temperatures paradoxically dampen increases in extreme humid-heat. *Environ. Res. Lett.***14**, 084003 (2019).

[36] McKinnon, K.A., Poppick, A. & Simpson, I.R. Hot extremes have become drier in the United States Southwest. *Nat. Clim. Chang.***11**, 598–604 (2021).

[37] Derbyshire, S.H. *et al.* Sensitivity of moist convection to environmental humidity. *Q. J. R. Meteorol. Soc.***130**, 3055-3079(2004).

[38] De Rooy, W.C. *et al.* Entrainment and detrainment in cumulus convection: An overview. *Q. J. R. Meteorol. Soc.***139**, 1-19(2013).

[39] Sherwood, S.C., & Nishant, N. Atmospheric changes through 2012 as shown by iteratively homogenized radiosonde temperature and wind data (IUKv2). *Environ. Res. Lett.* **10** 054007(2015).

[40] Mears, C.A. & Wentz, F.J. Sensitivity of satellite-derived tropospheric temperature trends to the diurnal cycle adjustment. *J. Clim.* **29** 3629-3646(2016).

[41] Caesar, J., Alexander, L., & Vose, R. Large-scale changes in observed daily maximum and minimum temperatures: Creation and analysis of a new gridded data set. *J. Geophys. Res.* **111**, D05101(2006).

[42] Dunn, R.J. *et al.* Development of an updated global land in situ-based data set of temperature and precipitation extremes: HadEX3. *J. Geophys. Res. Atmos.* **125**, e2019JD032263(2020).

[43] Morice, C.P. *et al.* An updated assessment of near-surface air temperature change from 1850: The HadCRUT5 data set. *J. of Geophys. Res. Atmos.***126** e2019JD032361(2021).

Acknowledgements

Y.Z. and W.R.B. acknowledge support from the Miller Institute for Basic Research in Science at the University of California, Berkeley. W.R.B. acknowledges support by the U.S. Department of Energy, Office of Science, Office of Biological and Environmental Research, Climate and Environmental Sciences Division, Regional and Global Model Analysis Program, under Award DE-SC0019367.

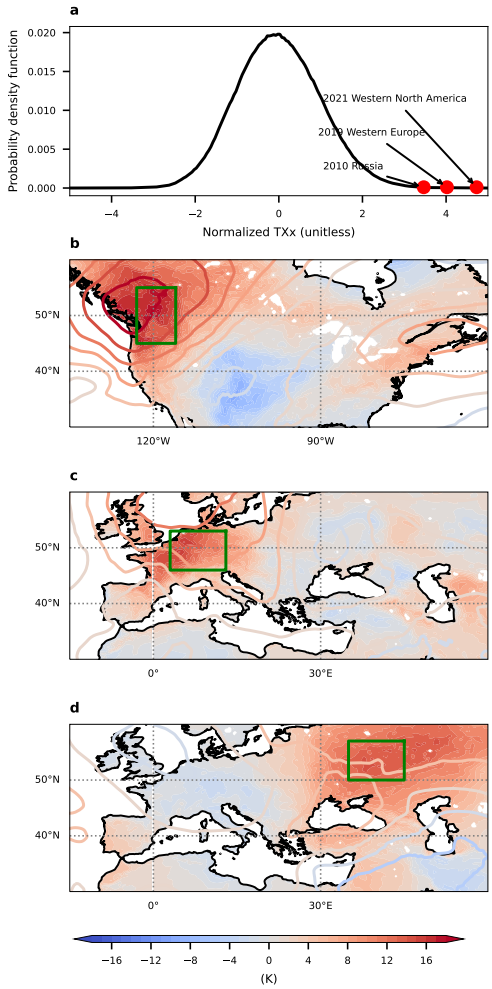

Figure 1: **Temperatures of recent mega-heatwaves. a**, Probability density distribution of normalized annual hottest daily maximum temperatures (TXx) over land between 40°N and 65°N for the period 1979-2021, and the maximum TXx during three mega-heatwaves as labelled. Normalized TXx is calculated location-wise by subtracting the average TXx from TXx then dividing the difference by the standard deviation of TXx for 1979-2021. **b-d**, Surface air temperature anomalies (color shading) and 500-hPa temperature anomalies (contours) during three mega-heatwaves, namely the 2021 Western North America heatwave (**b**), the 2019 European heatwave (**c**), and the 2010 Russian heatwave (**d**). Green boxes highlight the affected regions. Data are based on European Centre for Medium-Range Weather Forecasts Reanalysis 5 (ERA5) hourly data[32] on a $0.25° \times 0.25°$ grid.

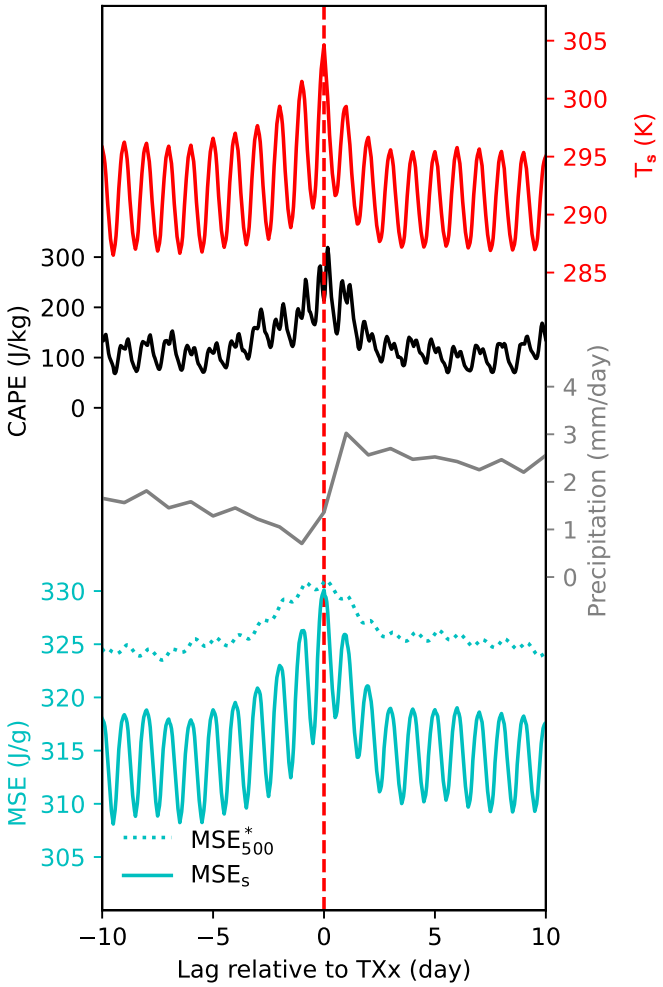

Figure 2: **Composite time series centered at annual hottest daily maximum temperatures (TXx).** Surface air temperature, convective available potential energy (CAPE), 2-meter moist static energy ($MSE_{surface}$), the saturation moist static energy at 500-hPa (MSE^*_{500}) are from hourly reanalysis of ERA5. Precipitation is from GPM daily observations. All time series shown are land averages between 40°N and 65°N of 2010.

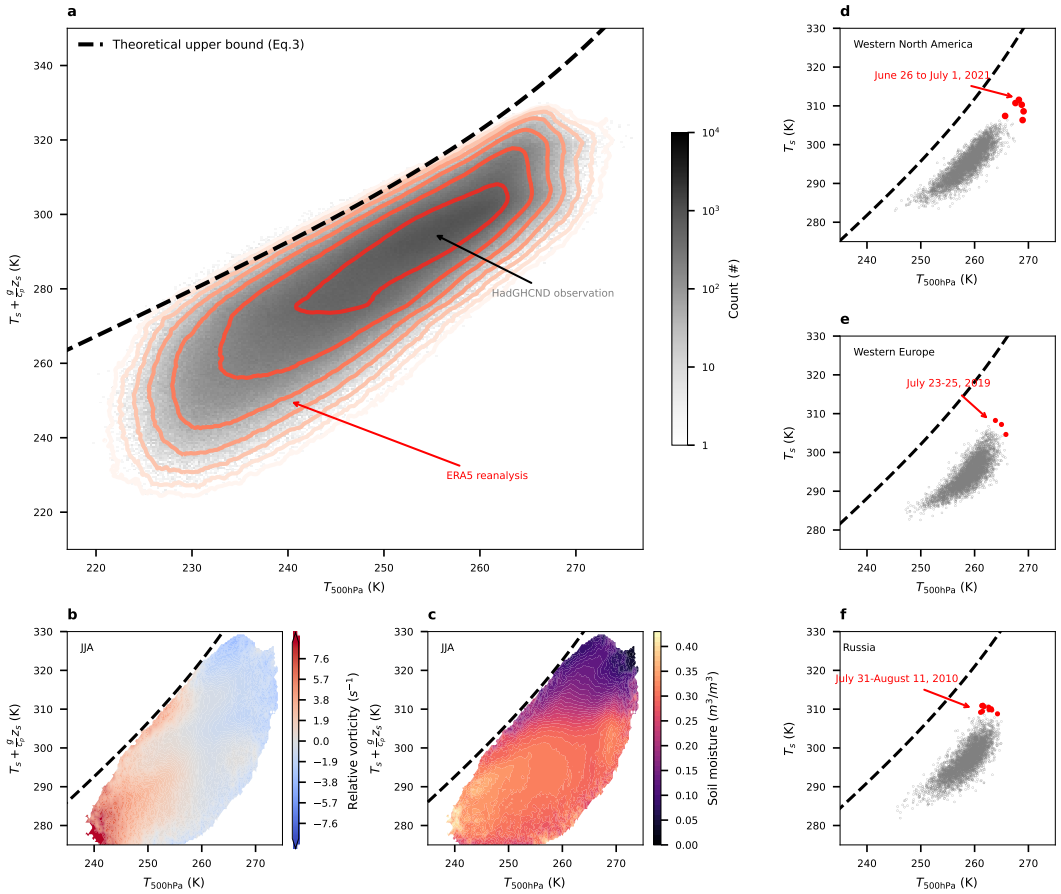

Figure 3: **Theory for the upper bound of surface air temperatures and evidence from observations and reanalysis data.** **a**, Theory for the upper bound of T_s (black dashed line) and joint histograms of daily-maximum temperatures (T_s) and daily-mean 500-hPa temperatures (T_{500}) over land between 40°N and 65°N for 2001-2021. T_{500} data are from the ERA5 reanalysis. T_s data are from Hadley Center Global Historical Climatology Network Daily data (HadGHCND)[41] ground observations (red contours) and the ERA5 reanalysis (grey shading). **b** Relative vorticity at 500 hPa as a function of T_{500} and T_s for June, July, and August (JJA) of 2001-2021. **c**, Same as **b** but for the surface-layer (0-7 mm) volumetric soil water content. **d-f**, T_s and T_{500} relationship over the three regions within the green boxes in Fig. 1b-d for JJA of 2001-2021.

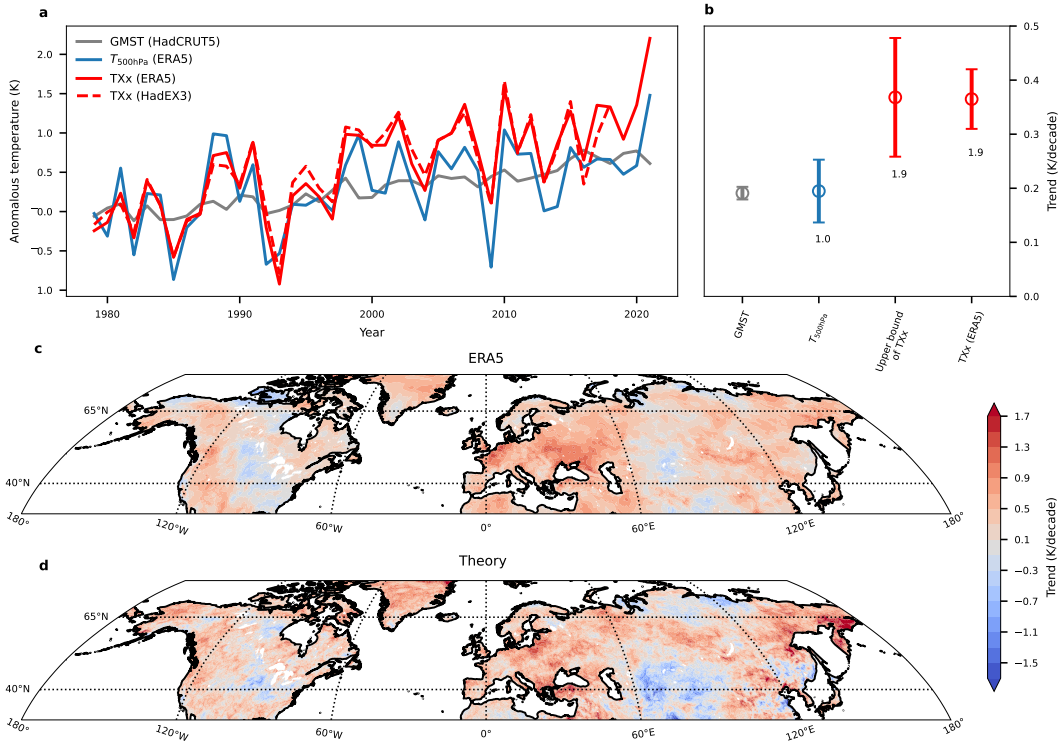

Figure 4: **Trends of annual hottest daily maximum temperature (TXx) in agreement with theory.** **a**, Time series of the global mean surface air temperature (GMST) from HadCRUT5 (gray), and the 40°N-65°N land average of TXx from ERA5 (red solid) and from HadEX3 (red dashed), and T_{500} on the annual hottest days from ERA5. **b**, Trends of GMST, T_{500} on annual hottest days, the upper bound of T_s, and TXx from ERA5 from 1979 to 2021. Confidence intervals for the linear trends represent 95% significance. Ratios of these trends to the GMST trend over the same period are annotated. **c**, Location-specific trends of TXx from 1979 to 2021 based on ERA5. **d**, Same as **c** but for the calculated trends in the upper bound of T_s from theory.

Extended Data

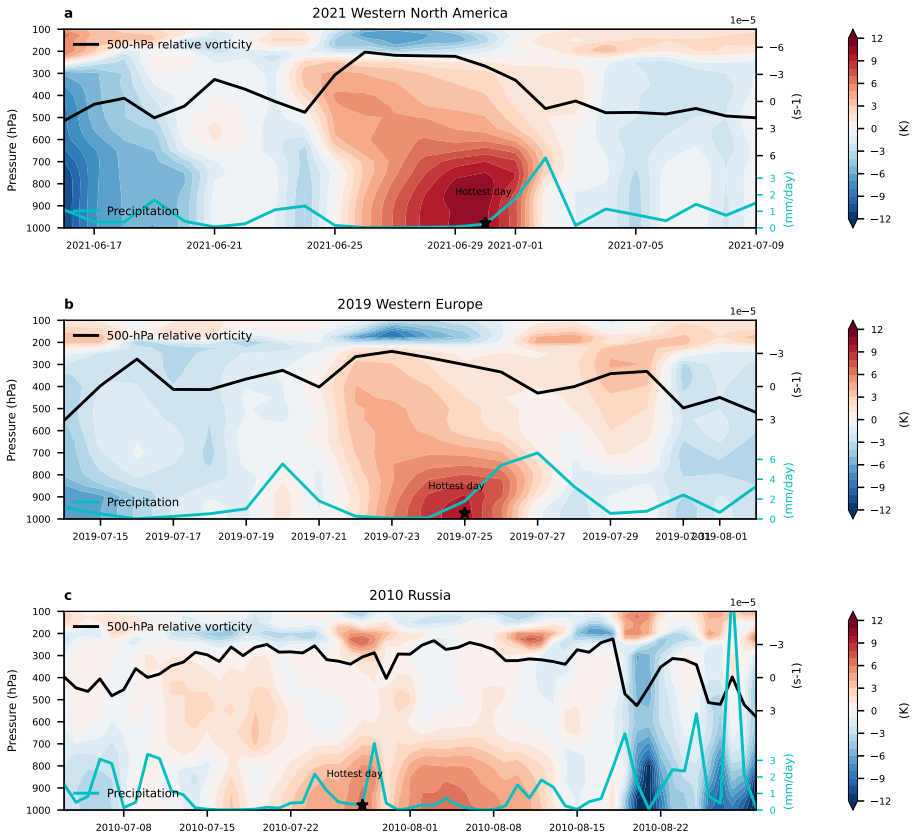

Extended Data Figure 1: **Time series of three heatwaves**. **a** Daily maximum tropospheric temperature anomalies (color shading), 500-hPa relative vorticity (black line), and precipitation (cyan line) during the 2021 Western North America heatwave. The same time series are shown for the 2019 Western European heatwave in **b** and the 2010 Russian heatwave in **c**. Average daily-maximum temperature for each vertical level over the shown time periods are subtracted to emphasize the anomalies. Borders of the three regions are the green boxes in Fig. 1b,c,d. Temperature and relative vorticity data are from ERA5, and precipitation data are from GPM.

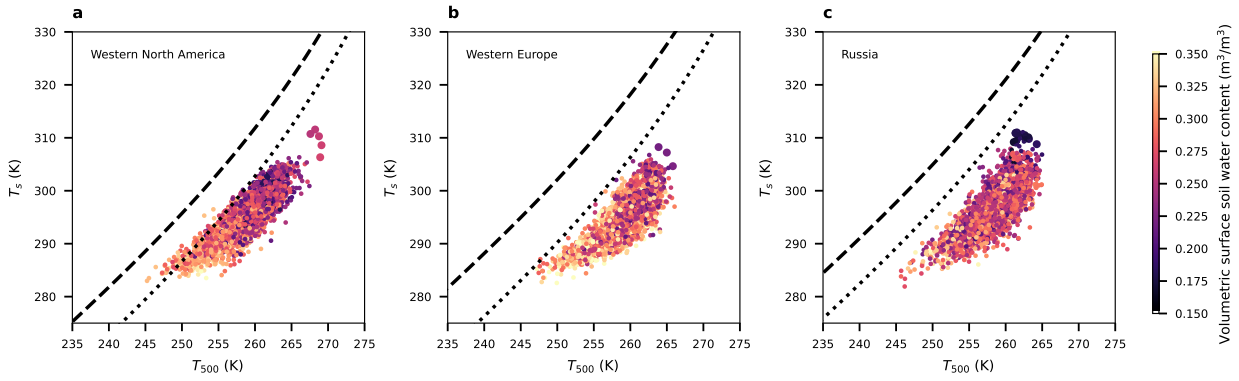

Extended Data Figure 2: The surface-layer (0-7 mm) volumetric soil water content for June-August from 1979 to 2021 as a function of T_{500} and T_s for (**a**) Western North America, (**b**) Western Europe, and (**c**) Russia. Dashes lines are the theoretical upper bound of T_s as in equation (3) and dotted lines are the upper bound subtracted by the minimum 2-m specific humidity for these regions.

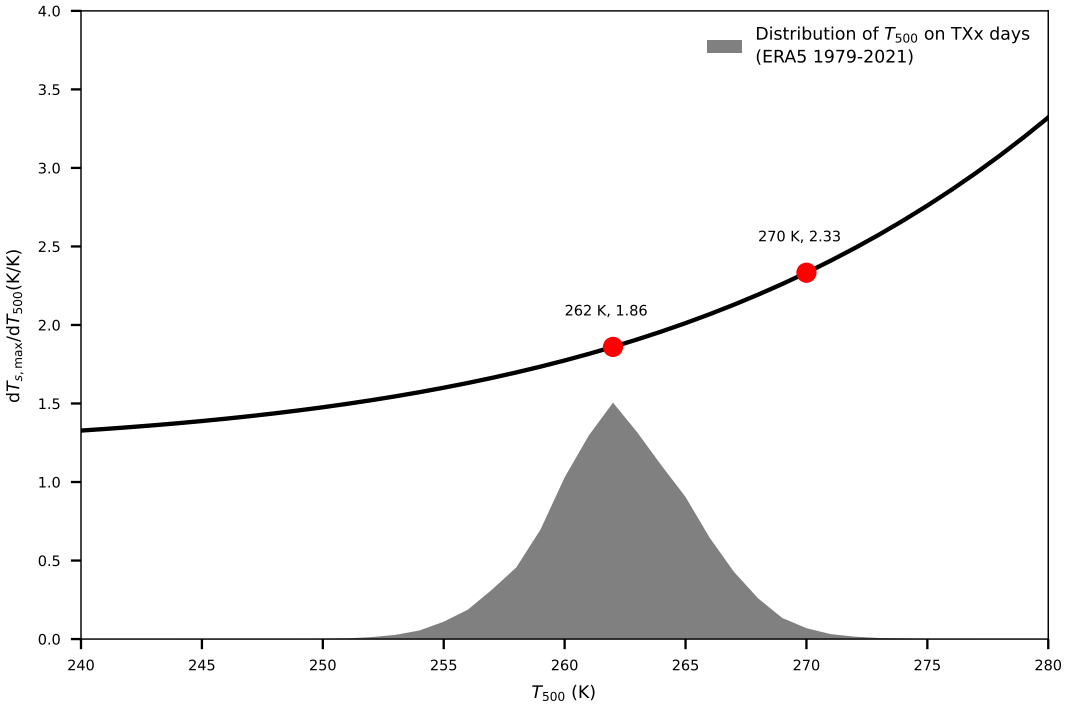

Extended Data Figure 3: **The increase of the upper bound of T_s per unit warming of T_{500}.** The distribution of T_{500} on annual hottest days from 1979 to 2021 based on ERA5 reanalysis is shown.

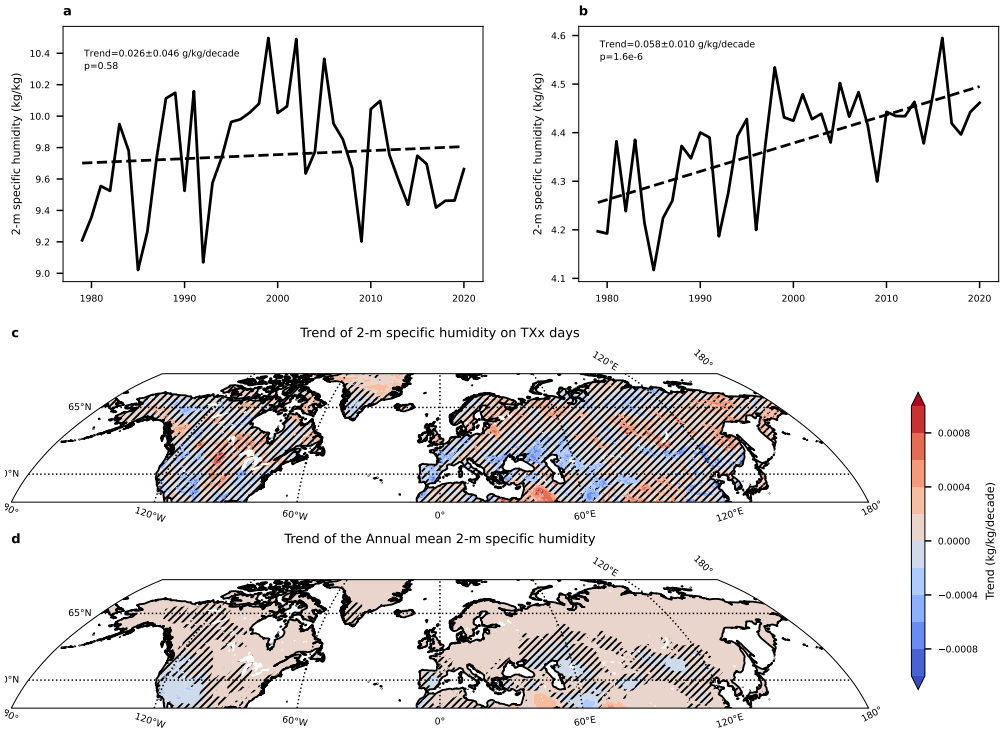

Extended Data Figure 4: **Trends in the surface (2-meter) air specific humidity.** The time series of **a**, 2-m specific humidity on TXx days and **b**, annual-mean 2-m specific humidity averaged over land between 40°N and 65°N. The location-specific trends of **c**, 2-m specific humidity on TXx days and **d**, annual-mean 2-m specific humidity. Hatched regions are those where the local null hypothesis can not be rejected on a 0.05 significance level.

Data set	Time period	Trend normalized by global warming
ERA5 T_{500} on TXx days (land)	1979-2021	1.0 ± 0.3
ERA5 annual mean T_{500} (land&ocean)	1979-2020	1.0 ± 0.2
IUKv2 annual mean T_{500} (land)	1979-2012	1.2 ± 0.4
MSU/AMSU TMT channel (land&ocean)	1979-2020	0.9 ± 0.1
MSU/AMSU TTT channel (land&ocean)	1979-2020	1.1 ± 0.1

Table 1: Average trends of T_{500} between 40°N and 65°N normalized by global warming for multiple data sets. For IUKv2 radiosondes, only the 123 sites with more than 80% of data available during 1979-2012 are included. Error bars are calculated as propagation of uncertainties using the 95% confidence interval of linear trends of T_{500} and global mean surface air temperature assuming the independence of the two variables.